Supporting Information for "Improved constraints on northern extratropical CO_2 fluxes obtained by combining surface-based and space-based atmospheric CO_2 measurements"

B. Byrne[1], J. Liu[2], M. Lee[2], I. Baker[3], K. W. Bowman[2], N. M. Deutscher[4], D. G. Feist[5,6,7], D. W. T. Griffith[4], L. T. Iraci[8], M. Kiel[2], J. S. Kimball[9], C. E. Miller[2], I. Morino[10], N. C. Parazoo[2], C. Petri[11], C. M. Roehl[12], M. K. Sha[13], K. Strong[14], V. A. Velazco[4], P. O. Wennberg[12,15], and D. Wunch[14]

[1]NASA Postdoctoral Program Fellow, Jet Propulsion Laboratory, California Institute of Technology, CA, USA

[2]Jet Propulsion Laboratory, California Institute of Technology, CA, USA

[3]Atmospheric Science Department, Colorado State University, Fort Collins, CO, USA

[4]Centre for Atmospheric Chemistry, University of Wollongong, Wollongong, Australia

[5]Max Planck Institute for Biogeochemistry, Jena, Germany

[6]Lehrstuhl fur Physik der Atmosphare, Ludwig-Maximilians-Universitat Munchen, Munich, Germany

[7]Institut fur Physik der Atmosphare, Deutsches Zentrum fur Luft- und Raumfahrt, Oberpfaffenhofen, Germany

[8]Atmospheric Science Branch, NASA Ames Research Center, Moffett Field, CA 94035, USA

[9]Numerical Terradynamic Simulation Group, W.A. Franke College of Forestry & Conservation, The University of Montana, Missoula, MT 59812, USA

[10]Satellite Observation Center, Center for Global Environmental Research, National Institute for Environmental Studies (NIES), 16-2 Onogawa, Tsukuba, Ibaraki 305-8506, Japan

[11]Institute of Environmental Physics, University of Bremen, Bremen, Germany

[12]Division of Geological and Planetary Sciences, California Institute of Technology, Pasadena, CA, USA

May 6, 2020, 12:12am

[13]Royal Belgian Institute for Space Aeronomy (BIRA-IASB), Brussels, Belgium

[14]Department of Physics, University of Toronto, Toronto, Ontario, Canada

[15]Division of Engineering and Applied Science, California Institute of Technology, Pasadena, CA, USA

Contents of this file

Text S1. Here we describe the posterior NEE fluxes obtained in the tropics and southern hemisphere. Figure S7 shows the net annual fluxes and mean seasonal cycle of NEE and biomass burning across four latitude bands. This is a reproduction of Fig. 4 from Crowell et al. (2019) using the results of this study. Note that the results from Crowell et al. (2019) are for 2015–2016, thus the fluxes should not be expected to be the same. The posterior fluxes in the northern extratropics are roughly consistent with the results of Crowell et al. (2019). In the northern and southern tropics, we obtain a larger spread in the posterior seasonal cycle than the ensemble of Crowell et al. (2019), which may be due to less observation coverage of GOSAT over the tropics. We find that GOSAT

Corresponding author: B. Byrne, Jet Propulsion Laboratory M/S 233-200, 4800 Oak Grove Drive, Pasadena, CA 91109. (brendan.k.byrne@jpl.nasa.gov)

measurements tend to increase the net source in the northern tropics and the sink in the southern tropics, consistent with the impact of OCO-2 in Crowell et al. (2019). However, the magnitude of this effect is smaller, which could be due to less observational coverage from GOSAT (partially due to the fact that we do not assimilate medium gain nadir observations).

Figures S8–S10 show the mean seasonal cycle of NEE, annual net NEE, and IAV in NEE for six regions in the tropics and southern hemisphere. The regions that we examine are tropical South America (12 °S–28 °N, 27.5–122.5 °W), tropical Africa (12 °S–28 °N, 27.5°W–62.5°E), tropical Asia (12 °S–28 °N, 62.5–180 °W), southern South America (12–90 °S,27.5–122.5 °W), southern Africa (12–90 °S, 27.5°W–62.5°E), and Australia (12–90 °S, 62.5–180 °W). In general, we find that the spread in the mean posterior NEE fluxes remains quite large for assimilated datasets, suggesting that there may not be sufficient observational coverage to constrain these regions. Previous studies have argued that ocean glint measurements are important for constraining tropical fluxes Deng-2016,Byrne-2017,Byrne-2019. In the southern extratropics (defined here as south of 12 °S), the GOSAT+surface+TCCON flux inversion provides reasonable precise estimates os seasonal and annual fluxes. IAV in NEE is found to be quite precise for a given assimilated dataset, however, the posterior IAV between assimilated datasets is generally not consistent, similar to the results found for northern extratropical regions.

References

Crowell, S., Baker, D., Schuh, A., Basu, S., Jacobson, A. R., Chevallier, F., ... Jones, D. B. A. (2019). The 2015–2016 carbon cycle as seen from OCO-2 and the global in situ network. *Atmos. Chem. Phys.*, *19*(15), 9797–9831. doi: 10.5194/acp-19-9797

-2019

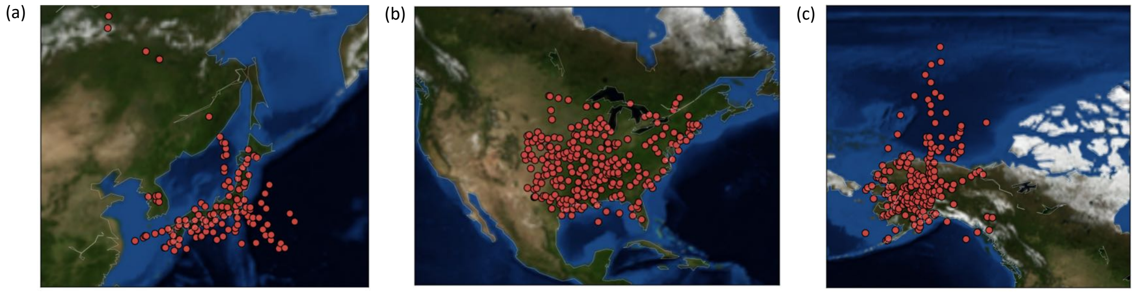

Figure S1. Locations of aircraft observations used in this study for (a) East Asia, (b) North America, and (c) Alaska/Arctic.

Table S1. Mean and standard deviation (std) of data–model mismatch between each flux inversion and aircraft-based CO_2 observations over East Asia, North America, and Alaska/Arctic. Posterior-simulated-CO_2 was calculated at $4° \times 5°$ spatial resolution.

Region		East Asia		North America		Alaska/Arctic	
data set	prior NEE	mean (ppm)	std (ppm)	mean (ppm)	std (ppm)	mean (ppm)	std (ppm)
prior	SiB3	-0.06	0.85	0.08	0.97	-0.84	1.61
	CASA	-0.01	0.76	0.26	0.56	-0.59	1.36
	FLUXCOM	1.18	0.70	1.54	0.57	1.24	1.00
	Mean NEE	0.37	0.57	0.63	0.54	-0.06	1.16
TCCON	SiB3	0.16	0.46	0.33	0.43	-0.10	0.86
	CASA	0.33	0.74	0.65	0.57	-0.02	1.30
	FLUXCOM	0.42	0.45	0.42	0.45	-0.02	1.18
	Mean NEE	0.30	0.42	0.43	0.47	-0.05	1.05
surface-only	SiB3	0.01	0.44	0.34	0.35	-0.06	0.80
	CASA	0.13	0.71	0.48	0.50	-0.14	1.22
	FLUXCOM	0.22	0.60	0.46	0.33	-0.01	0.88
	Mean NEE	0.12	0.43	0.43	0.31	-0.07	0.93
GOSAT-only	SiB3	0.25	0.41	0.49	0.37	-0.06	0.76
	CASA	0.14	0.36	0.43	0.36	-0.17	0.81
	FLUXCOM	0.23	0.44	0.50	0.33	0.03	0.89
	Mean NEE	0.21	0.33	0.47	0.32	-0.06	0.79
GOSAT	SiB3	0.18	0.35	0.34	0.31	-0.7	0.75
+surface	CASA	0.15	0.39	0.42	0.36	-0.03	0.89
+TCCON	FLUXCOM	0.16	0.38	0.39	0.32	0.00	0.93
	Mean NEE	0.16	0.31	0.38	0.32	-0.03	0.84

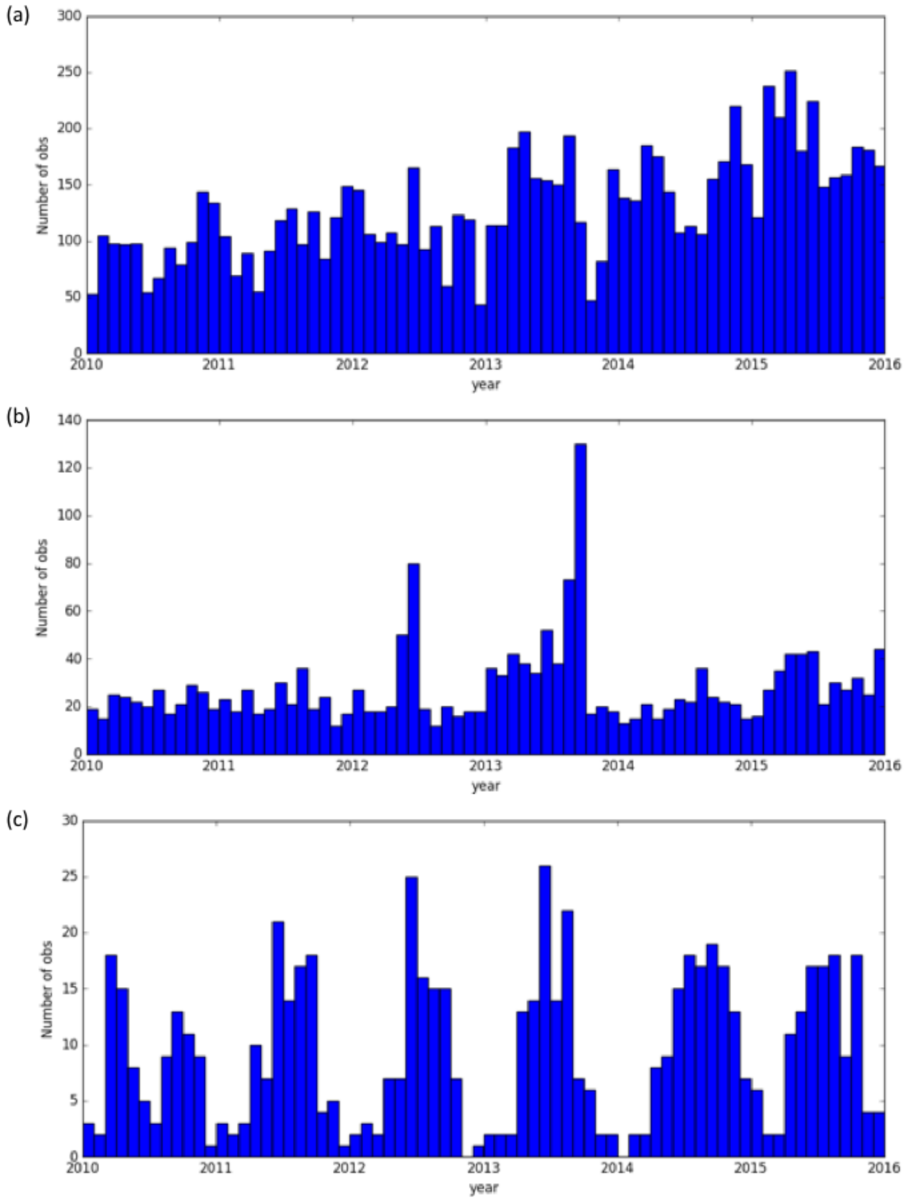

Figure S2. Number of hourly-mean aircraft measurements between 3–8 km altitude above sea level per month for (a) East Asia, (b) North America, and (c) Alaska/Arctic.

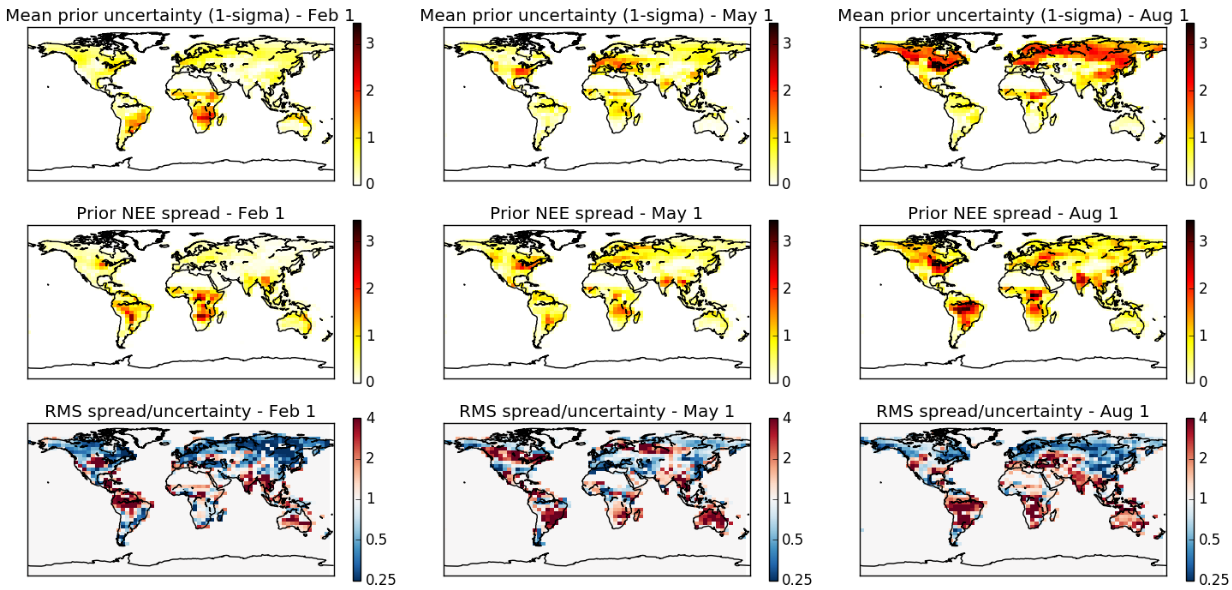

Figure S3. Comparison of prior uncertainty and prior NEE spread for (left column) Feb 1, (middle column) May 1, and (right column) Aug 1. The top row shows the 1-sigma mean model uncertainty in the prior fluxes ($\mathrm{gC\,m^{-2}\,day^{-1}}$), second row shows the spread (max minus min), and the bottom row shows the root-mean-square ratio of the model spread to prior uncertainty.

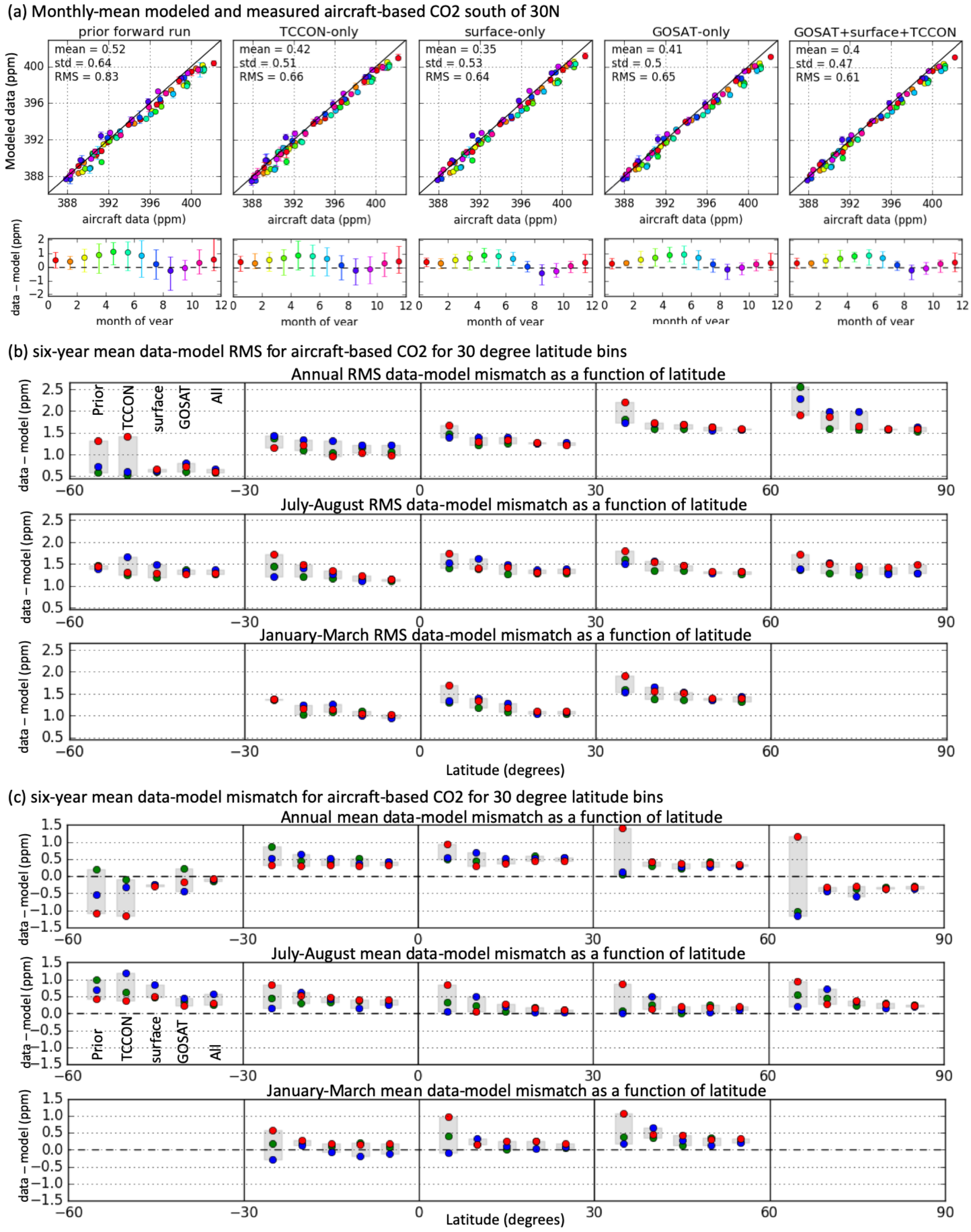

Figure S4. Comparison of posterior-simulated CO_2 and aircraft measurements between 3–8 km altitude for the tropics and southern hemisphere. (a) Same as Fig. 3 but for all aircraft measurements south of 30 ∘N. (b) RMS data-model mismatch for 30° latitude bins for (top) the entire year, (middle) July-August, and (bottom) January-March. (c) Mean data-model bias for 30° latitude bins for (top) the entire year, (middle) July-August, and (bottom) January-March. Points are for individual inversions and shaded regions show the range as in Fig. 6 for (left-to-right) the prior, TCCON-only, surface-only, GOSAT-only, and GOSAT+surface+TCCON posterior fluxes.

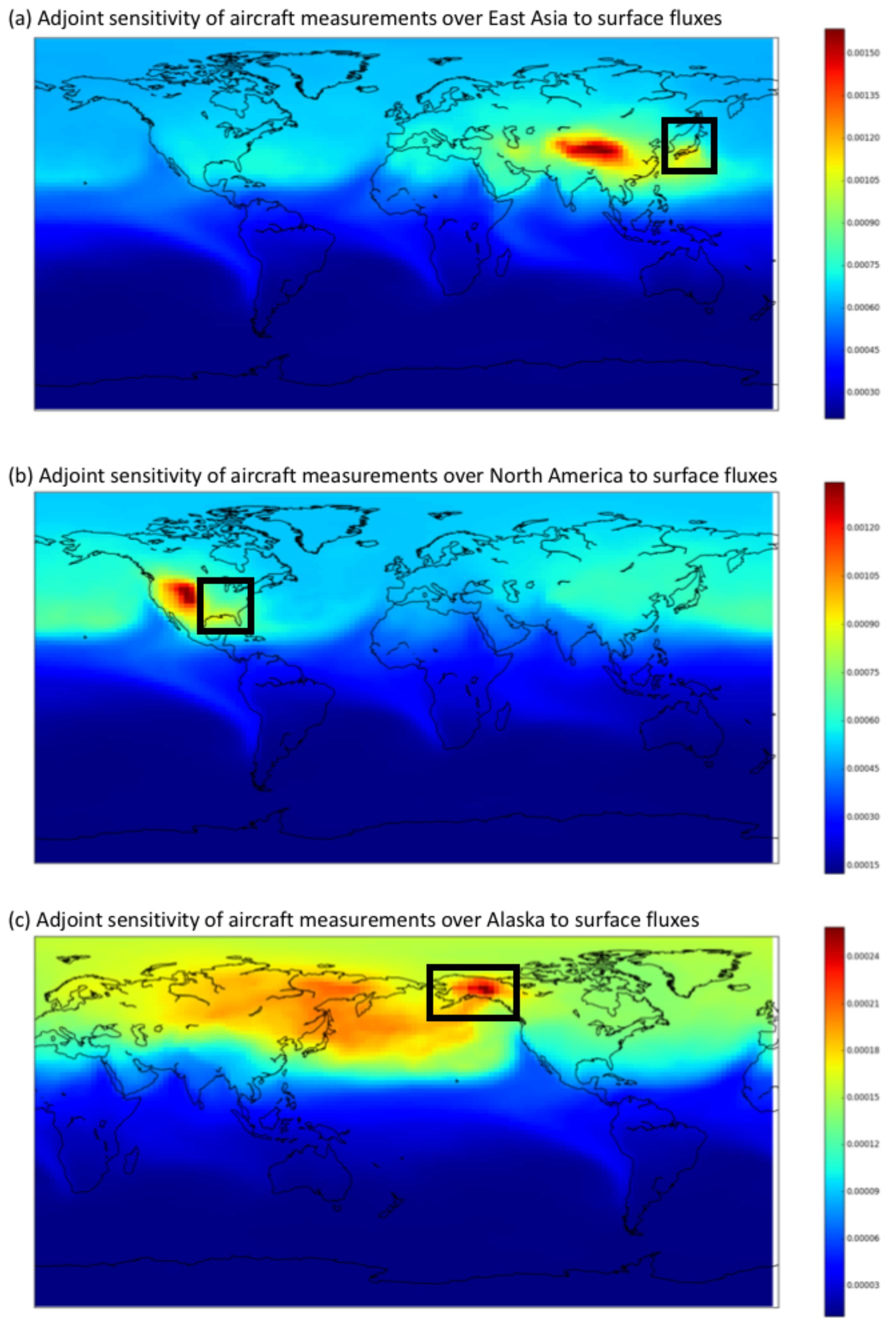

Figure S5. Adjoint sensitivity of aircraft-based CO_2 measurements to surface fluxes for measurements over (a) East Asia, (b) North America, and (c) Alaska/Arctic. Black boxes show the location of aircraft-based CO_2 measurements.

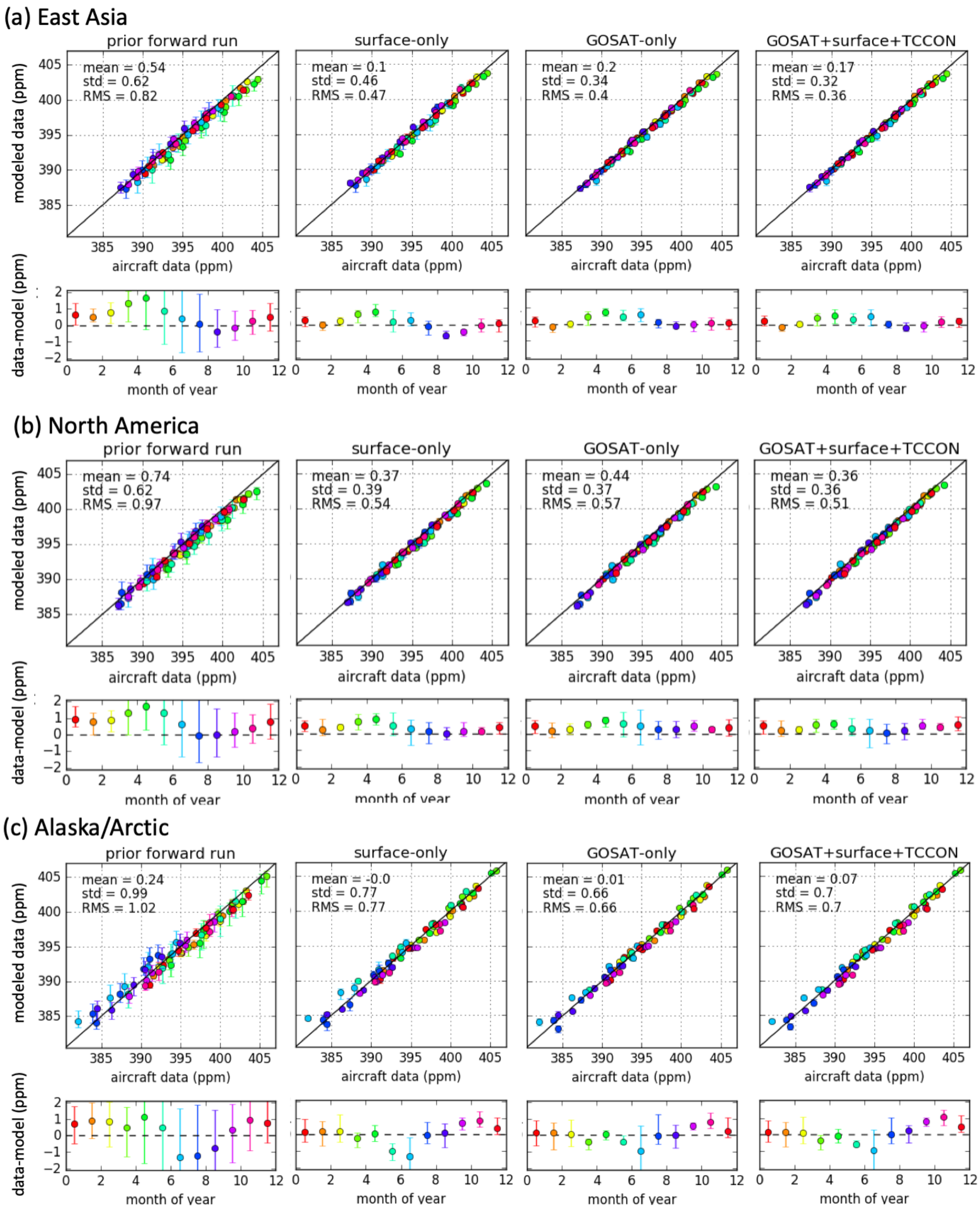

Figure S6. Same as Fig. 3 but at 2° × 2.5° spatial resolution (except for TCCON). Comparison of monthly mean measured and simulated aircraft-based CO_2 for (a) East Asia, (b) North America, and (c) Alaska/Arctic. For each region, the mismatch for (left to right) prior, surface-only, GOSAT-only, and GOSAT+surface+TCCON simulated CO_2 are shown. The top panel shows a scatter plot of the simulated aircraft-based CO_2 against the measured aircraft-based CO_2, and the error bars indicate the spread in posterior NEE. The lower panel shows the mean data–model mismatch for each month, with error bars showing the range of monthly mean mismatched over the six-years and inversion set-ups. Colors correspond to the month of year.

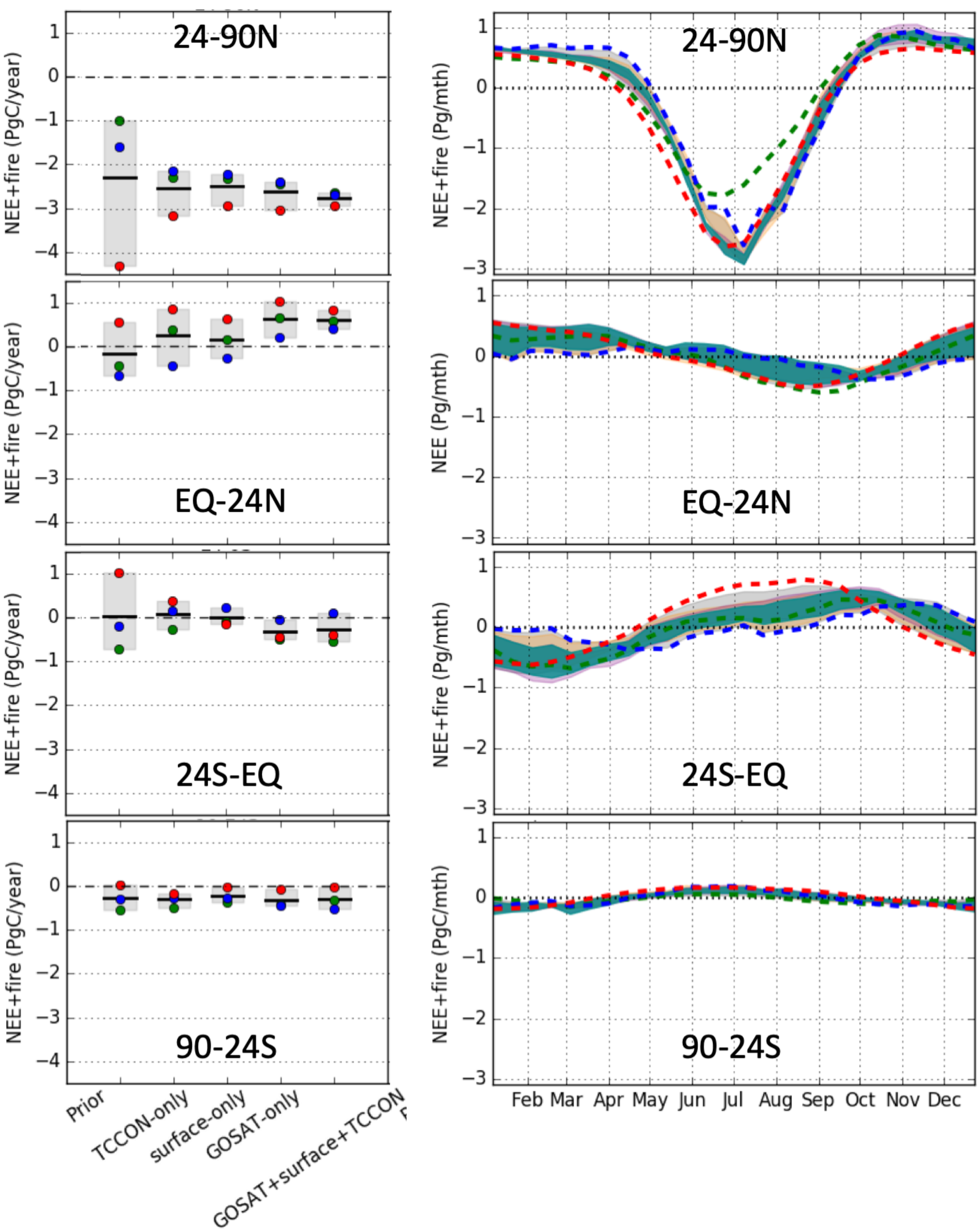

Figure S7. Mean 2010-2015 net flux and seasonal cycle of NEE + biomass burning over four latitude bands. This figure is reproduction of Fig. 4 from Crowell et al. (2019) using the results of this study. Six-year mean (left) annual net NEE and (right) seasonal cycle for all land between (top-to-bottom) 24–90 °N, 24–90 °N, 0–24 °S, 24–90 °S

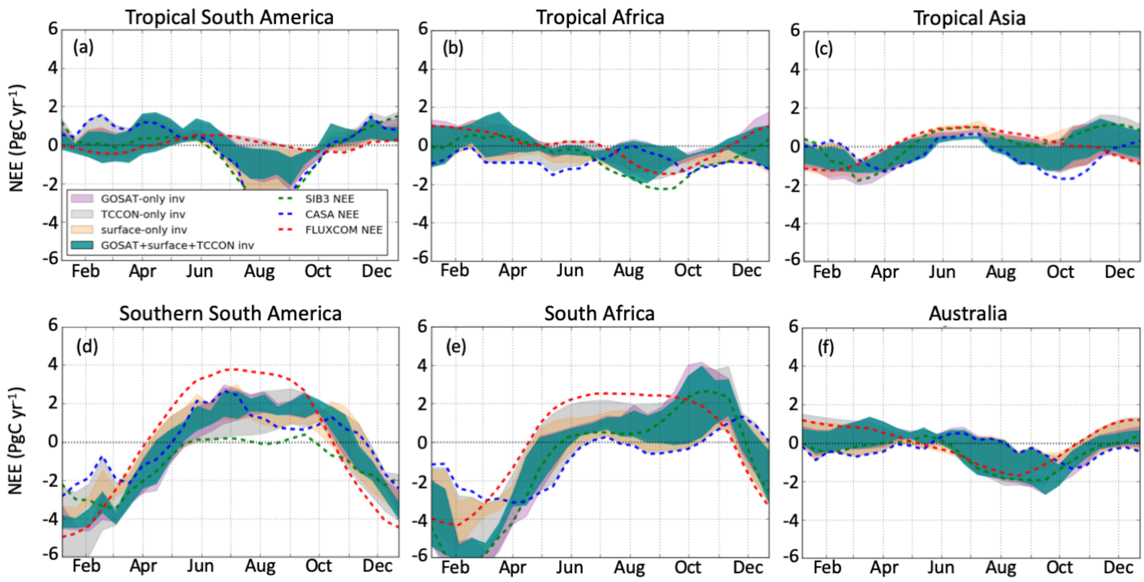

Figure S8. Same as Fig. 5 but for tropical and southern hemisphere regions.

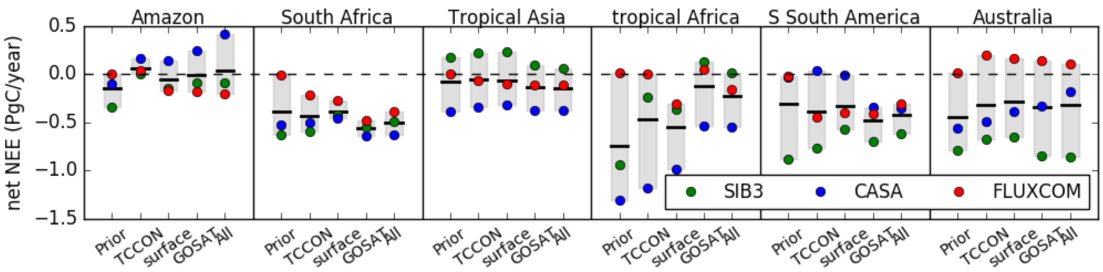

Figure S9. Same as Fig. 6 but for tropical and southern hemisphere regions.

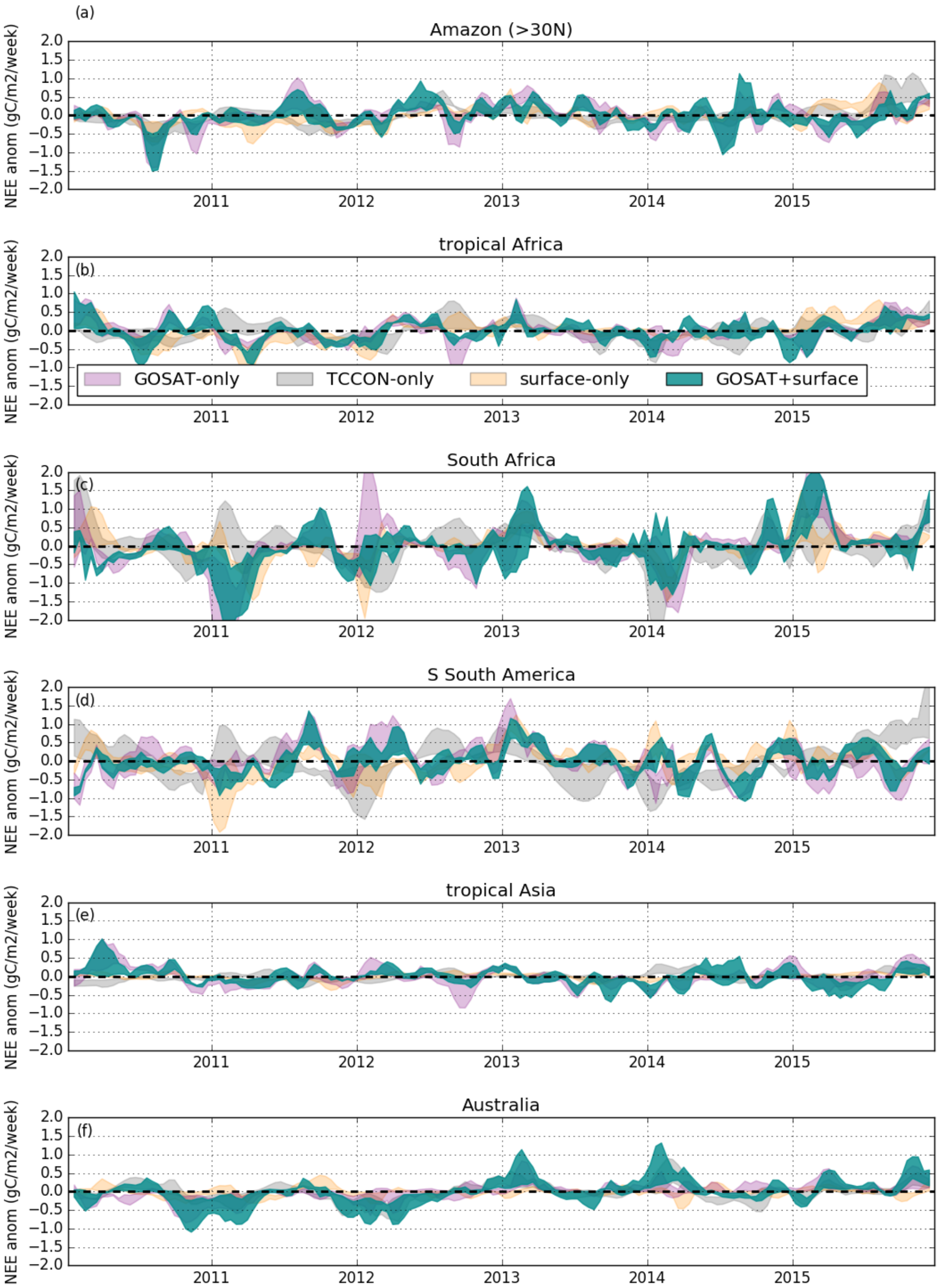

Figure S10. Same as Fig. 5 but for tropical and southern hemisphere regions.

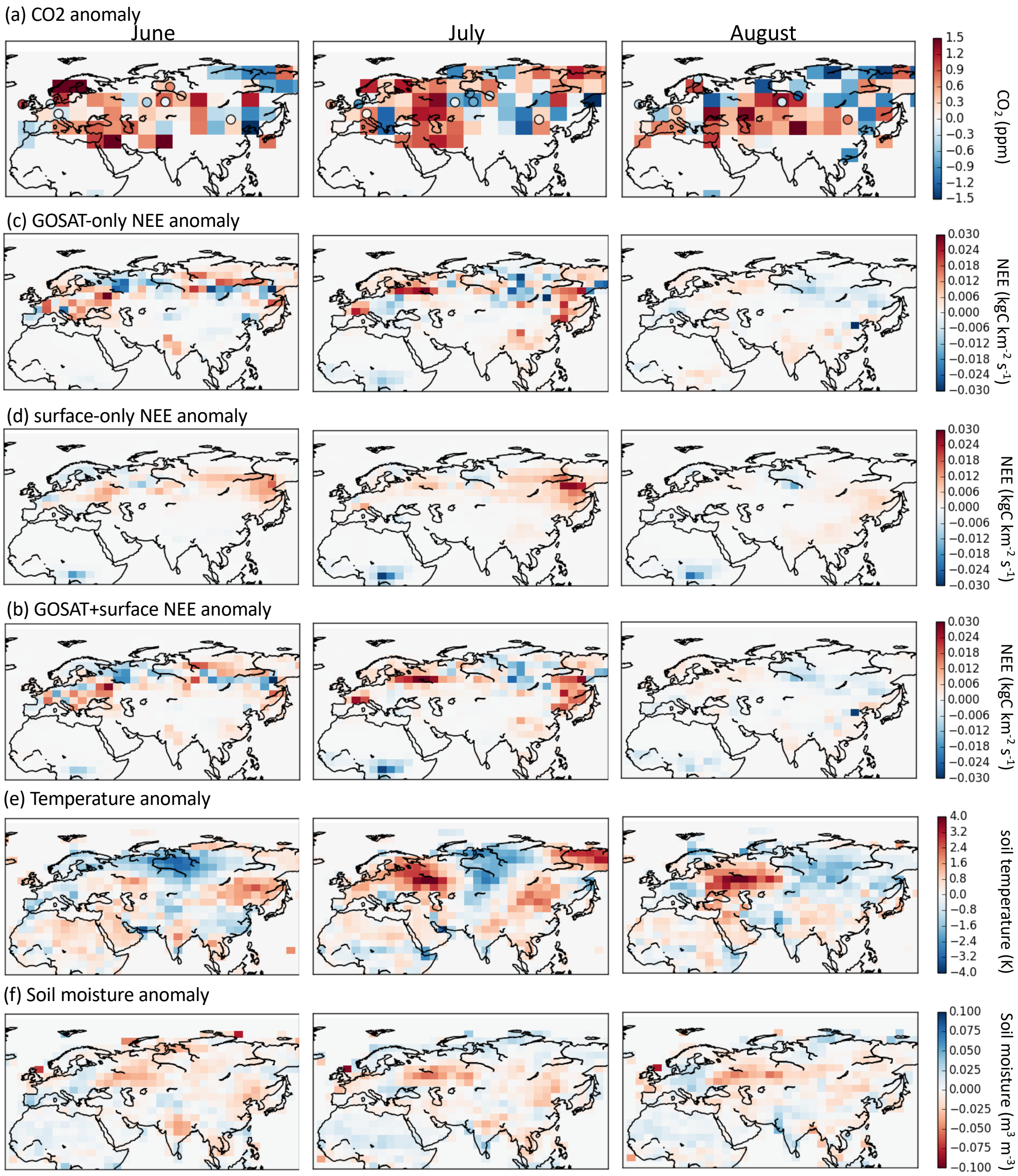

Figure S11. Same as Fig. 8 but for Eurasia during (left-to-right) May, June, July and August of 2010. Monthly anomalies in (a) GOSAT X_{CO_2} (ppm, $4° \times 5°$ grid cells) and surface site CO_2 (ppm divided by four, circles), (b) GOSAT-only posterior NEE, (c) surface-only posterior NEE, (d) GOSAT+surface posterior NEE, (e) MERRA-2 soil temperature anomalies (K), and (f) ESA CCI soil moisture.

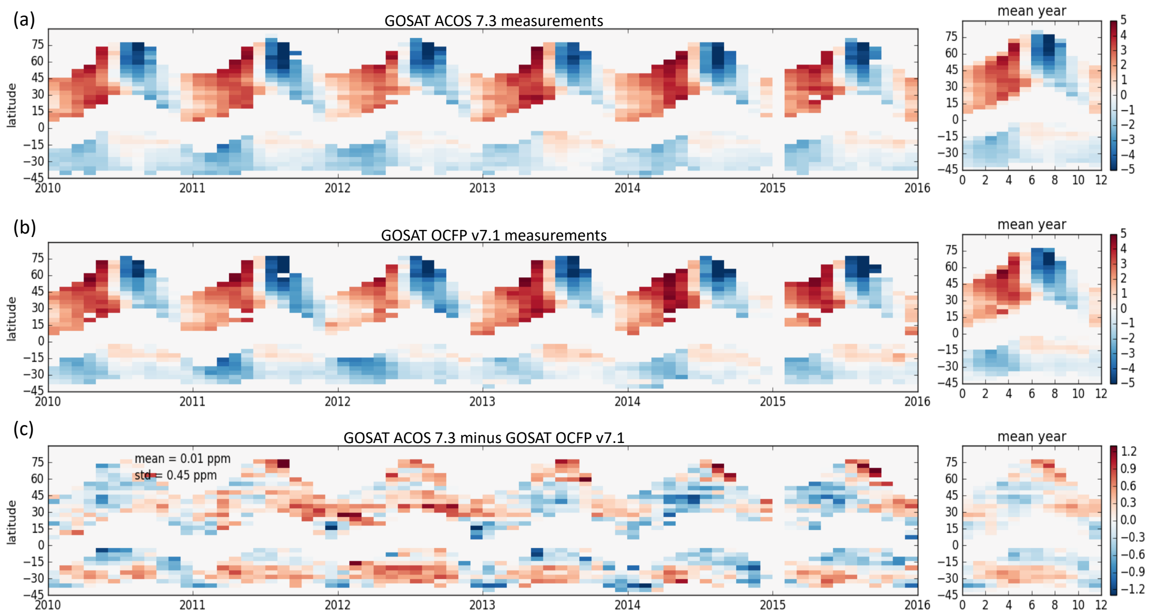

Figure S12. Detrended zonal-monthly mean high-gain nadir GOSAT X_{CO_2} retrieved by (a) ACOS 7.3 and (b) OCFP v7.1. (c) Difference in X_{CO_2} between the two retrieval algorithms.

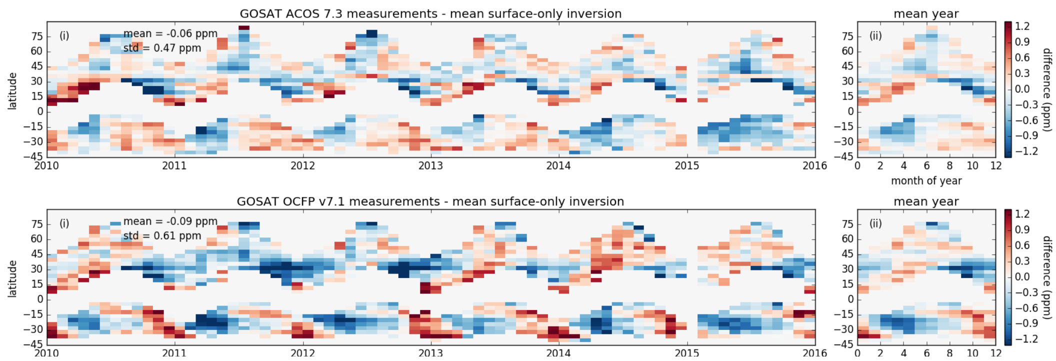

Figure S13. Data–model mismatch of the (a) ACOS 7.3 and (b) OCFP v7.1 GOSAT high-gain nadir X_{CO_2} measurements as a function of latitude and time for the surface-only flux inversion.

Table S2. Mean and standard deviation (std) of data–model mismatch between each flux inversion and aircraft-based CO_2 observations over East Asia, North America, and Alaska/Arctic. Posterior-simulated-CO_2 was calculated at $2^\circ \times 2.5^\circ$ spatial resolution.

Region		East Asia		North America		Alaska/Arctic	
data set	prior NEE	mean (ppm)	std (ppm)	mean (ppm)	std (ppm)	mean (ppm)	std (ppm)
4prior	SiB3	0.57	0.94	0.56	1.03	0.01	1.56
	CASA	-0.05	0.73	0.18	0.57	-0.54	1.20
	FLUXCOM	1.16	0.75	1.39	0.62	1.19	0.90
	Mean NEE	0.56	0.62	0.71	0.60	0.22	1.00
surface-only	SiB3	0.01	0.44	0.26	0.40	0.03	0.73
	CASA	0.11	0.69	0.38	0.57	-0.06	1.04
	FLUXCOM	0.22	0.62	0.35	0.39	0.06	0.79
	Mean NEE	0.11	0.45	0.33	0.38	0.01	0.79
GOSAT-only	SiB3	0.25	0.38	0.42	0.38	0.03	0.65
	CASA	0.18	0.39	0.37	0.39	-0.07	0.72
	FLUXCOM	0.24	0.46	0.42	0.36	0.14	0.75
	Mean NEE	0.22	0.35	0.40	0.35	0.03	0.68
GOSAT	SiB3	0.20	0.37	0.28	0.33	0.06	0.66
+surface	CASA	0.15	0.40	0.33	0.39	0.04	0.78
+TCCON	FLUXCOM	0.22	0.38	0.36	0.32	0.15	0.78
	Mean NEE	0.19	0.33	0.32	0.32	0.08	0.72